

Raman scattering study of the orthorhombic-to-tetragonal phase transition of a Li_3ThF_7 crystal

M. A. S. Oliveira

Departamento de Física, ICEX, UFMG, C.P. 702, 30123-970 Belo Horizonte, MG, Brazil

J.-Y. Gesland

Université du Maine, Cristallogénese, 72017 Le Mans, France

M. A. Pimenta and R. L. Moreira

Departamento de Física, ICEX, UFMG, C.P. 702, 30123-970 Belo Horizonte, MG, Brazil

(Received 12 March 1999; revised manuscript received 17 June 1999)

Raman spectroscopy was used to study pulled Li_3ThF_7 single crystals between 298 and 403 K, using six special backscattering geometries. The observed Raman bands were very broad, owing to the disorder related to the statistical occupancy of the lithium sites (with a 3/4 probability). In spite of this, the symmetry rules are well respected assuming an average model with four lithium ions per chemical formula. The spectral evolutions show a structural phase transition occurring at 368 K. After peak deconvolution, we were able to determine and attribute most of the Raman modes corresponding to each phase. The results are compatible with the proposed orthorhombic ($Ccca$) to tetragonal ($P4/ncc$) structural phase transition, whose ferroelastic nature would be responsible for the appearance of an ordered microcracking pattern in this crystal.

[S0163-1829(99)01438-1]

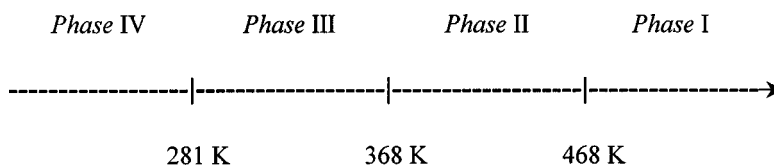
INTRODUCTION

Li_3ThF_7 crystal was prepared in 1959 by Thoma *et al.*¹ Since then, this crystal has attracted some attention, since the determination of its room temperature structure was rather complicated. First, different tetragonal structures have been proposed by Thoma and co-workers: $P4/nmm$ or $P4/n$, and by Cousson *et al.*: $P4/ncc$.^{2,3} Using valence-bond analysis and taking into account the anomalous Li-Li distances, Pauling⁴ showed that the previous structures were incorrect, although he did not propose an alternative one. The determination of an acceptable structure for this crystal was made only in 1989, by Laligant *et al.*,⁵ using x-ray and neutron-diffraction techniques. These authors showed that the correct room-temperature structure should belong to the orthorhombic $Ccca$ group.

Later, Laligant's group used neutron diffraction to show that the crystal presents a structural phase transition above room temperature, to a tetragonal structure ($P4/ncc$).⁶ This result was in agreement with previous differential thermal analysis measurements by Senegas and Pulcinelli,⁷ which found a thermal anomaly at about 341 K. The structures proposed for both phases have an interesting peculiarity: the lithium ions occupy randomly only 3/4 of their Wyckoff positions, which explains the observed high ionic conductivity

above room temperature, mainly in the **ab** plane.^{6,8-11}

Beside these fundamental questions concerning its structure, Li_3ThF_7 offers the unique feature of an inorganic x-ray monochromator for the 6.5 Å region. In view of this application, good quality samples of large dimensions are needed, which are not attained with the flux method used by other authors. Then, we are currently using the Czochralski method to grow large Li_3ThF_7 single crystals. This method allows us to obtain good quality crystals of about 10 cm³ volume. Nevertheless, during the cooling down to room temperature, the samples develop many cracks, irrespective of the cooling rates used. The lack of sufficient experimental data concerning the physical properties of this material, including studies about the above-mentioned phase transition, induced us to perform more thorough investigations of the material in a large temperature interval. In a very recent paper, we reported our dielectric, thermal, and conductivity studies on pulled Li_3ThF_7 single crystals.¹¹ The results were very surprising: while we confirmed the high ionic conduction of the crystal, we demonstrate the existence of three phase transitions in the temperature interval 100–800 K. The transitions are all displacive and of first-order type. The diagram below illustrates the proposed phase transition sequence of this crystal:



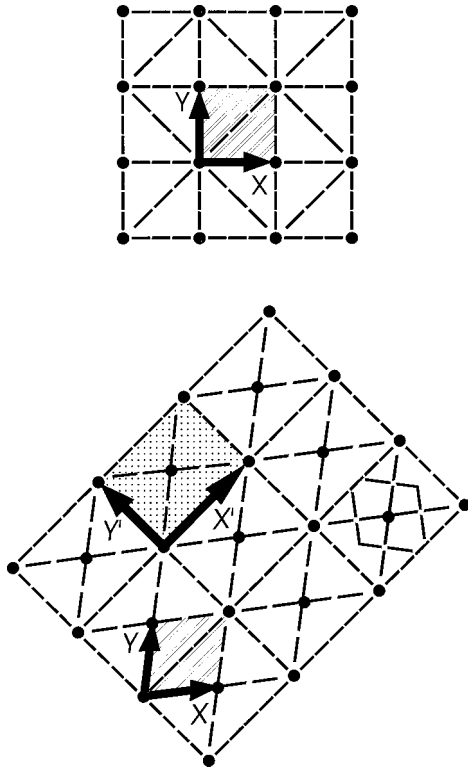


FIG. 1. \mathbf{XY} -plane projection (sketch) of the primitive unit cell (hatched), the face-centered-orthorhombic cell (with points) and the primitive Wigner-Seitz cell (gray) for phase III. The tetragonal unit cell (hatched) is also shown in the top of the figure.

The Laligant's transition was found at 368 K, 27 K above the temperature reported in Refs. 6 and 7, where flux-grown polycrystals were used. Nevertheless, the other features reported for this transition seems to hold. The crystal symmetry is clearly tetragonal in phases I and II (henceforth PI and PII), and lower than tetragonal in phases III and IV ($PIII$ and PIV). In fact, in spite of the controversy generated by the existence of, at least, two different phases in the phase diagram above, structural and birefringence experiments carried out in $PIII$ and PII are well compatible with the orthorhombic $Ccca$ and tetragonal $P4/ncc$ Laligant's structures, respectively. The situation of the two different phases PI and PIV is more complicated, since they are structurally very similar to PII and $PIII$ respectively. This explains why these phases were not detected in previous studies.^{5,6} The results of our structural investigations will be published elsewhere.

In this paper, we focus on the orthorhombic-to-tetragonal

TABLE I. Crystallographic characteristics of the phases III and II of Li_3ThF_7 . Z represents the number of motifs per unit cell. Structural data according to Refs. 5 and 6.

	P III $D_{2h}^{22}-Ccca$	P II D_{4h}^8-P4/ncc
Space Group		
Unit-cell basis	$\mathbf{a}' = \mathbf{a}_{III} = \mathbf{a}_{II} - \mathbf{b}_{II}$ $\mathbf{b}' = \mathbf{b}_{III} = \mathbf{a}_{II} + \mathbf{b}_{II}$ $\mathbf{c}_{III} = \mathbf{c}_{II}$	$\mathbf{a} = \mathbf{a}_{II}$ $\mathbf{b} = \mathbf{b}_{II}$ \mathbf{c}_{II} ($a_{II} = b_{II}$)
Z	8	4

TABLE II. Symmetry classification of the Γ zone-center optical modes for the phases III and II of Li_3ThF_7 . The acoustic modes have been omitted. The formula unit contains four Li ions.

	P III D_{2h}^{22}	P II D_{4h}^8
Raman-active modes	16 A_g 18 B_{1g} 19 B_{2g} 19 B_{3g}	9 A_{1g} 8 B_{1g} 7 B_{2g} 19 E_g
Infrared-active modes	17 B_{1u} 18 B_{2u} 18 B_{3u}	9 A_{2u} 18 E_u

($PIII$ - PII) phase transition, since the spontaneous elastic strain accompanying this transition is surely related to the multiple cracks that develop in the crystal. At this phase transition, the unit cell is doubled, with the orthorhombic \mathbf{X}' and \mathbf{Y}' axes making an angle of 45° with the corresponding tetragonal ones,⁶ as shown in Fig. 1. Table I summarizes the main structural characteristics of these phases.

In order to contribute to the understanding of the $PIII$ - PII transition, we have performed a systematic investigation of the Raman spectral evolutions of a pulled crystal, in the temperature range 298–403 K. In fact, some characteristic features of this system, like the fractional occupancy of lithium sites and the rotation of the unit-cell basis during the transition, make the Raman spectroscopy an interesting tool to investigate the crystal's behavior. In particular, we report the attributions of the Raman modes in both $PIII$ and PII phases.

EXPERIMENTAL PROCEDURES

Large Li_3ThF_7 single crystals have been grown by the Czochralski method. This crystal melts congruently at 843 K. In its preparation, lithium fluoride (LiF) was first purified and pulled from the melt in a fluorinating atmosphere. Thorium fluoride (ThF_4) was synthesized by fluorination of thorium oxide (ThO_2), using ammonium hydrogen difluorid

TABLE III. Raman irreducible representations and the corresponding cross sections (intensities) for the scattering geometries used, in phases III and II. The Raman tensor elements (a to f , according to the notation of Ref. 12) are expressed with respect to the axes of each corresponding phase. X' and Y' are the principal axes of the orthorhombic phase. The symbol \oplus denotes symmetry mixture due to the 45° rotation of the crystallographic axes. w is the weighted fraction of the $Y'Y'$ domain in the $X'X'$ orientation.

Configuration	P III modes	Intensity	P II modes	Intensity
$Z(\mathbf{XX})\bar{Z}$	$A_g \oplus B_{1g}$	$[(a+b)/2]^2 \oplus d^2$	$A_{1g} \oplus B_{1g}$	$a^2 \oplus c^2$
$Z(\mathbf{XY})\bar{Z}$	A_g	$[(a-b)/2]^2$	B_{2g}	d^2
$X(\mathbf{ZZ})\bar{X}$	A_g	c^2	A_{1g}	b^2
$X(\mathbf{ZY})\bar{X}$	$B_{2g} \oplus B_{3g}$	$e^2 \oplus f^2$	E_g	e^2
$Z(\mathbf{X}'\mathbf{X}')\bar{Z}$	A_g	$(1-w)a^2 + wb^2$	$A_{1g} \oplus B_{2g}$	$a^2 \oplus d^2$
$Z(\mathbf{X}'\mathbf{Y}')\bar{Z}$	B_{1g}	d^2	B_{1g}	c^2

TABLE IV. Correlation diagrams between the “gerad” irreducible representations of the D_{4h} group and those of its subgroup D_{2h} . A_{2g} is silent.

D_{4h}	→	D_{2h}
A_{1g}	→	A_g
B_{2g}	→	A_g
A_{2g}	→	B_{1g}
B_{1g}	→	B_{1g}
E_g	→	$\begin{cases} B_{2g} \\ B_{3g} \end{cases}$

(NH_4HF_2), and melted in a fluorinating atmosphere. Then, Li_3ThF_7 single crystals were pulled from stoichiometric mixtures ($3\text{LiF}+\text{ThF}_4$) in a platinum crucible, under a CF_4/HF /argon atmosphere. The first single crystals have been obtained by spontaneous growing germination on a platinum wire, followed by the classical necking selection. Then, large crystals were pulled from seeds, oriented, and cut along the $[110]$ tetragonal direction, which was found in the highest growth rate direction. During the cooling to room temperature, many little cracks appeared in all the crystals, even using very small cooling rates (0.5 K/min). The obtained Li_3ThF_7 crystals are easily cleaved perpendicularly to the $[001]$ direction.

In order to realize our studies, the crystals have been oriented, cut, and polished according to the principal axes of the high-temperature tetragonal phase (P_{II}). Typical samples used were approximately cubes with ~ 5 mm each side. After optical polishing, the samples have been observed in polarized optical microscopy at room temperature, showing optical birefringence in the \mathbf{ab} plane (in agreement with the proposed orthorhombic symmetry for this phase). This technique showed also the existence of 90° domains, separated very often by cracks, lying parallel to the tetragonal axes, i.e., accompanying the domain walls. Nevertheless, most of the observed cracks are situated at 45° of these axes, i.e., parallel to the (P_{III}) orthorhombic \mathbf{a}' , \mathbf{b}' axes, rotated of 45° around \mathbf{c} .⁶ All the cracks contain the \mathbf{c} axis. Concerning the high-temperature P_{II} , the observations between po-

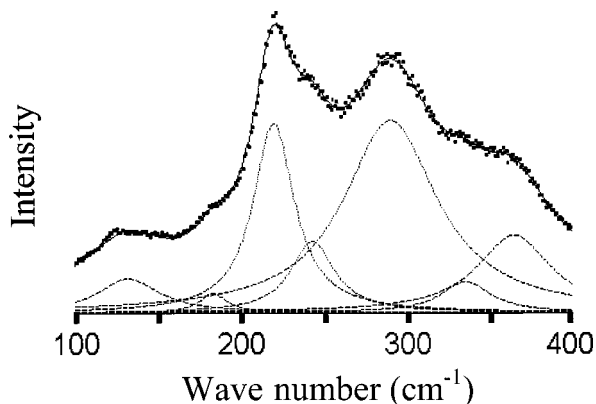


FIG. 2. Typical fitting of a Li_3ThF_7 Raman Spectra, in the $Z(XY)\bar{Z}$ scattering geometry, in the tetragonal phase. The standard sum of Lorentzian lines was used.

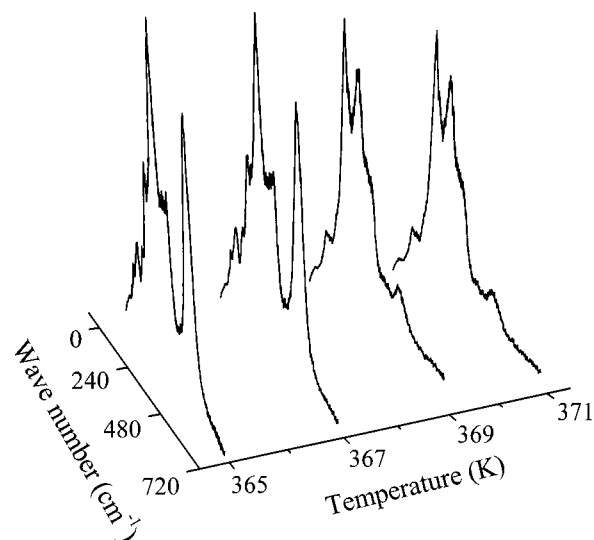


FIG. 3. Temperature dependence of the Raman spectra of a Czochralski grown Li_3ThF_7 single crystal, in the $Z(XY)\bar{Z}$ configuration, around the orthorhombic-to-tetragonal phase transition.

larizers show the optical isotropy in the \mathbf{ab} plane, in agreement with the proposed tetragonal symmetry.

The Raman spectra were recorded with a Dilor XY Raman triple monochromator spectrometer equipped with a multiarray detector (resolution: ~ 2 cm^{-1}). The 514.5 nm (500 mW) line of an argon-ion laser (COHERENT INNOVA 70) was used as the exciting source. The experiments were performed in backscattering configuration, in the temperature range 298–403 K, with absolute temperature accuracy better than 1 K.

PRELIMINARY GROUP THEORY CONSIDERATIONS

Taking into account the space groups of the proposed structures for Li_3ThF_7 crystal for its P_{III} ($Ccca$) and P_{II} ($P4/ncc$) phases, and their nonpolar nature, we can use either backscattering or the right angle Raman configurations, with no loss of information. We decided to use the backscattering configuration, since it is less sensitive to the cracks of the samples in the \mathbf{ab} plane. In order to verify the necessary scattering geometries to our Raman study around the P_{III} - P_{II} transition, we need to use Group Theory tools to predict the number of active Raman modes and their symmetries. However, due to the fractional occupancy of $3/4$ lithium ions in the structure, strictly speaking, the crystallographic unit cells of Refs. 5 and 6 are rather average ones, i.e., the true translational property of the crystal is perturbed by this disorder. Nevertheless, as will become clear in the next section, the Raman spectra denote obedience to the Raman-scattering selection rules, if we consider that each lithium site is occupied by lithium ions, i.e., if we take four Li^+ per chemical formula. Assuming this hypothesis, group-theoretical analysis of the normal vibrational modes at the Γ point becomes possible.

Besides the above features, we need also to consider that the orthorhombic crystallographic unit cell for phase III ($Ccca$) is not a primitive cell. Figure 1 shows the projection in the XY plane of the primitive cell, the face-centered-orthorhombic cell and the primitive Wigner-Seitz cell for

TABLE V. Frequencies ($\bar{\nu}$) and damping constants (Γ) for the modes of the tetragonal phase (P II) of Li_3ThF_7 . p indicates polarization leaks.

$Z(XX)\bar{Z}:A_{1g}\oplus B_{1g}$		$Z(XY)\bar{Z}:B_{2g}$		$X(ZZ)\bar{X}:A_{1g}$		$X(ZY)\bar{X}:E_g$		$Z(X'X')\bar{Z}:A_{1g}\oplus B_{2g}$		$Z(X'Y')\bar{Z}:B_{1g}$	
$\bar{\nu}(\text{cm}^{-1})$	$\Gamma(\text{cm}^{-1})$	$\bar{\nu}(\text{cm}^{-1})$	$\Gamma(\text{cm}^{-1})$	$\bar{\nu}(\text{cm}^{-1})$	$\Gamma(\text{cm}^{-1})$	$\bar{\nu}(\text{cm}^{-1})$	$\Gamma(\text{cm}^{-1})$	$\bar{\nu}(\text{cm}^{-1})$	$\Gamma(\text{cm}^{-1})$	$\bar{\nu}(\text{cm}^{-1})$	$\Gamma(\text{cm}^{-1})$
96 ^a	16	133	55	133	40	140	23	106	22	96	16
106	22	184	20	151	23	169	33	133	40	139	52
134	40	221	30	170(p)	36	220	27	150	23	188	28
149	23	244	32	217	30	250	38	184 ^b	20	208	25
186 ^a	28	291	68	255	46	287	44	222 ^b	30	226	27
281	46	336	36	282	46	312	30	244 ^b	32	249	32
342	40	365	54	340	40	331	30	283	46	291	66
374 ^a	40			496	44	354	44	342	40	374	40
497	44					475	40	372(p)	46		
524	30					501	56	497	44		
								524	30		

^aModes of B_{1g} symmetry.^bModes of B_{2g} symmetry.

phase III. Also shown in this figure is the unit cell of phase II. Notice that the two twofold axes lying in the XY plane of the orthorhombic phase III are no more parallel to the tetragonal X and Y axes. In fact, they are along the X' and Y' directions, which are rotated by $\sim 45^\circ$ from X and Y . The symmetrically correct primitive cell for the lattice in such a case is the Wigner-Seitz cell,¹² whose principal axes are parallel to X' and Y' (note also that, for this cell, $Z=4$). Then we applied the factor-group method,^{12,13} based on the ionic positions determined by the Laligant's group,^{5,6} to determine the number and assignment of the vibrational modes for the phases III and II, presented in Table II (the acoustic modes have been excluded).

The irreducible representations for both groups are those of their own principal axes (a property of the Wigner-Seitz cell). As we discussed above, the X' , Y' principal axes of the orthorhombic cell are situated at 45° of the tetragonal X , Y ones. Physically, the 45° rotation of axes accounts for the dependence of the tensorial properties on the point-group symmetry (the Raman scattering depends on second-order polarizability tensors). We take the benefit of this peculiarity to choose special geometries, which give additional information concerning the vibrational mode assignment in both phases. Table III presents the scattering geometries used in this work (with Porto's notation¹⁴), as well as the symmetries of the corresponding modes and their cross sections. Note

TABLE VI. Frequencies ($\bar{\nu}$) and damping constants (Γ) for the modes of the orthorhombic phase (P III) of Li_3ThF_7 . p indicates polarization leaks.

$Z(XX)\bar{Z}:A_g\oplus B_{1g}$		$Z(XY)\bar{Z}:A_g$		$X(ZZ)\bar{X}:A_g$		$X(ZY)\bar{X}:B_{2g}\oplus B_{3g}$		$Z(X'X')\bar{Z}:A_g$		$Z(X'Y')\bar{Z}:B_{1g}$	
$\bar{\nu}(\text{cm}^{-1})$	$\Gamma(\text{cm}^{-1})$	$\bar{\nu}(\text{cm}^{-1})$	$\Gamma(\text{cm}^{-1})$	$\bar{\nu}(\text{cm}^{-1})$	$\Gamma(\text{cm}^{-1})$	$\bar{\nu}(\text{cm}^{-1})$	$\Gamma(\text{cm}^{-1})$	$\bar{\nu}(\text{cm}^{-1})$	$\Gamma(\text{cm}^{-1})$	$\bar{\nu}(\text{cm}^{-1})$	$\Gamma(\text{cm}^{-1})$
89	10	88	9	88	10	94	17	90	8	101	18
106	14	107	14	151	18	138	17	107	14	128	17
125	18	125	18	157(p)	14	155	14	140	18	141	18
139 ^a	18	139(p)	18	173	14	169	26	151	16	150	14
151	16	150	16	216	19	219	26	173	14	159	24
184	20	185	20	255	28	232	16	183	20	192	18
191 ^b	18	216	18	268(p)	19	249	32	218	19	215	20
216	18	224	18	228(p)	23	269	24	226	19	243	22
224	18	253	26	348	24	286	24	282	24	257	18
254	26	282	24	363	20	304	22	299	22	284	26
282	24	297	22	496	30	319	18	316	22	297	19
297	22	311(p)	23	519	20	333	22	349	24	310	22
312 ^b	23	348	24			357	32	363	20	356	26
350	24	363	20			436	26	498	32	377	26
363	20	377(p)	24			458	20	519	20		
377 ^b	24	496	30			480	28				
497	32	519	20			499	28				
520	20					523	24				

^aModes of mixed symmetries A_g+B_{1g} .^bModes of B_{1g} symmetry.

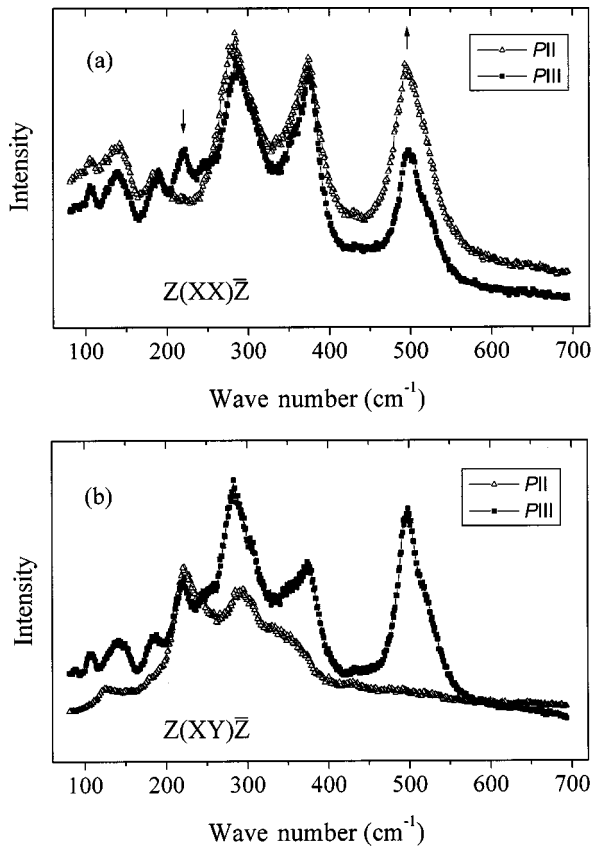


FIG. 4. Observed Phase III (298 K, solid squares) and Phase II (403 K, open triangles) Raman spectra of the Li_3ThF_7 crystal for (a) $Z(\overline{XX})\overline{Z}$ and (b) $Z(\overline{XY})\overline{Z}$ configurations. The arrows represent the increasing (up arrows) or decreasing (down arrows) of the intensity of some weaker bands.

that, besides the large number of Raman predicted modes of this crystal, we have mixture of symmetries (represented by \oplus) and of domains (represented by the weight factor w).

The present predictions allow us to explain the main features of the Raman spectra and to investigate the spectral changes around the phase transition, since the use of adequate scattering configurations lead, in some cases, to important changes in the Raman tensor elements. As we will present in the next section, this is particularly the case for the $Z(\overline{XY})\overline{Z}$ configuration, since the observed symmetry is B_{2g} in phase II and A_g in phase III. We remark that A_g modes cannot be observed in the $Z(\overline{X'Y'})\overline{Z}$ configuration but are the only modes detected in the $Z(\overline{XY})\overline{Z}$ configuration. This shows that one needs to take care with the analysis of quoted and unquoted scattering geometries. Finally, in order to help us to study the spectral evolution near the P_{III} to P_{II} phase transition, we give in Table IV the correlation diagram for the irreducible representations of the two proposed phases.

RESULTS AND DISCUSSIONS

The Raman spectra of Li_3ThF_7 single crystals have been recorded at the six scattering geometry's described in Table III, between 298 and 403 K. The bands exhibit rather large widths and are located always below 600 cm^{-1} , which is the usual case for these kinds of fluorine containing crystals. A

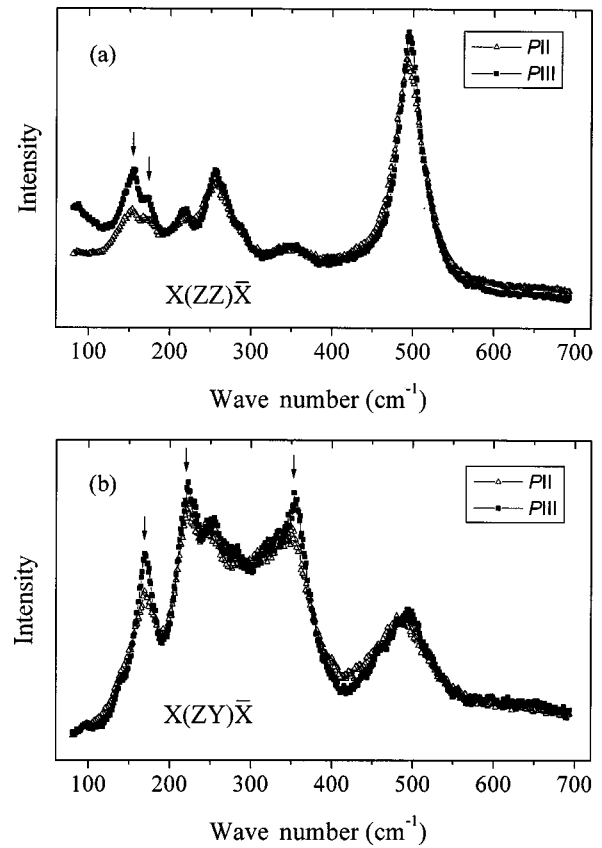


FIG. 5. Observed Phase III (298 K, solid squares) and Phase II (403 K, open triangles) Raman spectra of the Li_3ThF_7 crystal for (a) $X(\overline{ZZ})\overline{X}$ and (b) $X(\overline{ZY})\overline{X}$ configurations. The arrows have the same meaning as in the preceding figure.

possible explanation for the large widths of the bands should be linked to the statistical occupancy of the lithium positions, leading to some disorder in the structure (and to the high ionic conductivity observed for this crystal). Nevertheless, as it will be seen in the sequence, the system does not lose its main symmetry, and the general group-theory predictions concerning the symmetries hold in all cases. All the spectra presented in this study were divided out by the Bose factor $[n(\omega) + 1]$.¹⁵ After, they were fitted by a sum of Lorentzian lines. Figure 2 shows a typical fitting of the Raman spectra by means of the sum of Lorentzian lines. Since in this procedure we use a large number of parameters, some restrictions were adopted in the fitting process. For example, the A_g symmetry modes in phase III can appear in four different scattering geometries: $Z(\overline{XX})\overline{Z}$; $Z(\overline{XY})\overline{Z}$; $X(\overline{ZZ})\overline{X}$; $Z(\overline{X'X'})\overline{Z}$. Thus, we look for the modes which are present simultaneously in these configurations (the same frequencies and damping constants should appear in the four configurations, taking into account the 2 cm^{-1} resolution of the apparatus). In addition, the relative intensities of modes of a given representation should be the same in the different configurations. This kind of procedure was extended for all representations.

We first remark that, on heating the samples, all spectra (for all configurations) show no important evolution until 365 K (the band intensities and widths exhibit no remarkable changes). Between 365 and 371 K, the spectra show pronounced changes, which we associate to the orthorhombic to

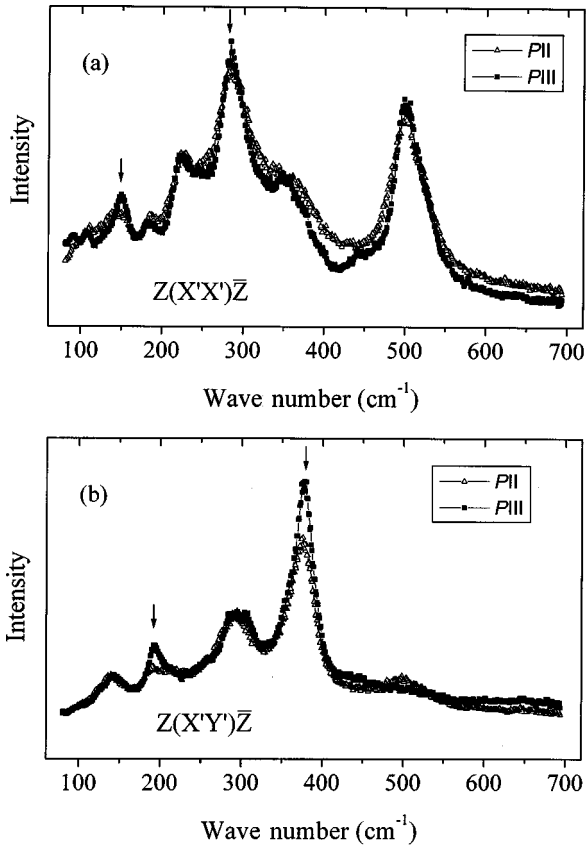


FIG. 6. Observed Phase III (298 K, solid squares) and Phase II (403 K, open triangles) Raman spectra of the Li_3ThF_7 crystal for (a) $Z(X'X')\bar{Z}$ and (b) $Z(X'Y')\bar{Z}$ configurations. The arrows have the same meaning as in the two preceding figures.

tetragonal phase transition. This result is exemplified in Fig. 3 for the $Z(XY)\bar{Z}$ configuration, where the most remarkable changes occur. Above this temperature until 403 K the spectra remain unchanged. Since the only changes occur around the critical temperature, we can compare directly the P_{III} and P_{II} temperature spectra for each configuration, in order to perform a more thorough analysis.

Let us now present the attribution of the vibrational modes, after the fitting procedure illustrated previously in Fig. 2, which has been applied to the spectra shown in Figs. 4–6. These figures present the complete set of spectra in the six scattering geometries used, for both P_{III} and P_{II} phases. We analyze first the obtained modes and we discuss later individual features of the spectra. Table V gives the frequencies and damping constants found for the tetragonal phase. Note that, for the $X(ZZ)\bar{X}$ configuration, seven of the nine A_{1g} expected modes were depicted. Nevertheless, the other two bands could be observed at 106 and 524 cm^{-1} in the $Z(XX)\bar{Z}$ and $Z(X'X')\bar{Z}$ configurations, completing thus the foreseen number. All the expected B_{1g} modes in $Z(X'Y')\bar{Z}$ and B_{2g} modes in the $Z(XY)\bar{Z}$ configuration could be found. In the $X(ZY)\bar{X}$ configuration, 10 of the 19 E_g expected modes could be observed. As a whole, these results present a good agreement with our assumption of four Li ions per chemical formula (otherwise, the number of predicted modes would be lower than that observed).

The frequencies and damping constants for the bands in

the orthorhombic phase are presented in Table VI. In this case, due to the absence of degenerate modes, the theory predicts a greater number of Raman bands than for the tetragonal phase. However, the number of depicted Raman bands is lower than we expected, although larger than for the tetragonal phase. We could detect all 16 expected A_g modes and 14 of the 18 anticipated B_{1g} ones. The B_{2g} and B_{3g} modes are seen together in the same Raman-scattering geometry, $X(ZY)\bar{X}$, and only 18 bands were observed (a half of the expected modes for these representations).

Now we present a more detailed discussion of the spectral evolution near the phase transition. Figure 4 gives the P_{III} (298 K, solid square) and P_{II} (403 K, open triangles) spectra for the Li_3ThF_7 crystal in the (a) $Z(XX)\bar{Z}$ and (b) $Z(XY)\bar{Z}$ configurations. Comparing first the room-temperature spectra for these two configurations [the solid squares of Figs. 4(a) and 4(b)], we observe that they are very similar, since they present mainly A_g modes, as seen in Table III. The differences between these spectra is mainly due to weaker B_{1g} modes, allowed in $Z(XX)\bar{Z}$ symmetry. Let us compare the room- and high-temperature spectra for each configuration. In the $Z(XX)\bar{Z}$ configuration, we observe the disappearance of two bands: 216 and 224 cm^{-1} , while a third band located at 497 cm^{-1} becomes stronger. These changes are indicated by the arrows in Fig. 4(a). The changes in the $Z(XY)\bar{Z}$ configuration are more drastic: the P_{II} spectrum is completely different from the P_{III} one. The former shows relatively a lower number of modes, since the 16 A_g modes (P_{III}) are divided into 7 B_{2g} and 9 A_{1g} ones (P_{II}). For the above configuration, the A_{1g} modes are not expected, which explains the observed reduction in the number of the measured Raman bands.

Figure 5 displays the spectra for the (a) $X(ZZ)\bar{X}$ and (b) $X(ZY)\bar{X}$ configurations. We first note that the P_{III} spectra for these two configurations are completely different, since they belong to different irreducible representations, respectively, A_g and $(B_{2g} \oplus B_{3g})$. On heating the sample, these modes transform, respectively, in the P_{II} representations A_{1g} and E_g , which are essentially linked to the same Raman tensor elements of the corresponding P_{III} representations (A_{1g} and A_g are the totally symmetric representations; the doubly degenerated E_g representation of the tetragonal phase leads to the B_{2g} and B_{3g} modes of the orthorhombic one). Thus, the changes in the spectra are very subtle: some low-frequency bands decrease in intensity in the high-temperature phase.

The P_{III} spectra for the $Z(X'X')\bar{Z}$ and $Z(X'Y')\bar{Z}$ configurations, presented, respectively, in Figs. 6(a) and 6(b), are completely different, since these scattering geometries allow the separation of the A_g and B_{1g} modes, which were superimposed in the $Z(XX)\bar{Z}$ and $Z(XY)\bar{Z}$ spectra presented in Fig. 4. Comparing the P_{III} and P_{II} quoted spectra for each configuration, we see that each of them present only small changes (still associated with the decreasing or vanishing of the intensities of some bands). As before, this can be explained by the corresponding symmetries of the Raman tensor elements (see Table III). The expected reduction of the number of modes on heating the sample above the P_{III} - P_{II} transition temperature is verified only after the peak

deconvolution, as shown in Tables V and VI.

The Raman results presented here clearly confirm the existence of an orthorhombic-to-tetragonal phase transition for a pulled Li_3ThF_7 single crystal at 368 K. The transition temperature is 27 K above that observed by other authors in polycrystals^{6,7} but agrees with our previous results in single crystals.¹¹ A possible reason for this discrepancy can be linked to the better quality of the Czochralski samples compared to those prepared by the flux method (where traces of LiTh_2F_9 were found).⁵

The above phase transition has a first-order character, as evidenced by thermal and structural results,^{6,11} but we did not discern any thermal hysteresis, within the experimental accuracy of our experiments (1 K). Moreover, its ferroelastic nature is certainly responsible for the appearance of many microcracks in the sample during the phase transition.

CONCLUSION

Raman spectroscopy has been used to investigate the spectral evolution of pulled Li_3ThF_7 single crystals, between 298 and 403 K. The results confirmed the existence of a

phase transition at 368 K, and are well compatible with the proposed change between a *Ccca* structure to a *P4/ncc* one. This transition has a first-order character (in spite of the absence of thermal hysteresis) and should be responsible for the appearance of many microcracks in the sample, owing to its ferroelastic nature. The observed Raman bands in both phases are very broad, which can be ascribed to the disorder associated with the statistical occupancy of the lithium sites (3/4). Although this disorder was always present, the assumption of an average four Li ions per chemical formula showed to be very acceptable and the general group-theory predictions concerning the symmetries hold in all cases. A detailed fitting of the Raman bands allowed us to attribute most of the vibrational modes, in good agreement with the group-theory predictions for an ordered crystal.

ACKNOWLEDGMENTS

This work has been partially supported by the Brazilian (CNPq and FAPEMIG) and French (CNRS) government agencies.

-
- ¹R. E. Thoma, H. Insley, B. S. Landau, H. A. Friedman, and W. R. Grimes, *J. Phys. Chem.* **63**, 1266 (1959).
²L. A. Harris, G. D. White, and R. E. Thoma, *J. Phys. Chem.* **63**, 1974 (1959).
³A. Cousson, M. Pages, and R. Chevalier, *Acta Crystallogr., Sect. B: Struct. Crystallogr. Cryst. Chem.* **34**, 1776 (1978).
⁴L. Pauling, *Acta Crystallogr., Sect. B: Struct. Crystallogr. Cryst. Chem.* **35**, 1535 (1979).
⁵Y. Laligant, A. Le Bail, D. Avignant, J. C. Cousseins, J. P. Battut, J. Dupuis, and M. Hamdi, *J. Solid State Chem.* **80**, 206 (1989).
⁶Y. Laligant, G. Ferey, M. El Ghozzi, and D. Avignant, *Eur. J. Solid State Inorg. Chem.* **29**, 497 (1992).
⁷J. Senegas and S. H. Pulcinelli, *J. Fluorine Chem.* **42**, 31 (1989).
⁸J. Senegas and S. H. Pulcinelli, *J. Fluorine Chem.* **38**, 375 (1988).
⁹S. H. Pulcinelli, R. H. de Almeida Santos, and J. Senegas, *J. Fluorine Chem.* **42**, 41 (1989).
¹⁰S. H. Pulcinelli and J. Senegas, *Eur. J. Solid State Inorg. Chem.* **25**, 249 (1988).
¹¹M. A. S. Oliveira, J.-Y. Gesland, and R. L. Moreira, *Phys. Rev. B* **56**, 7755 (1997).
¹²G. Turrel, *Infrared and Raman Spectra of Crystals* (Academic, London, 1972).
¹³D. L. Rousseau, R. P. Bauman, and S. P. S. Porto, *J. Raman Spectrosc.* **10**, 253 (1981).
¹⁴W. S. Otaguro, E. Wiener-Avnear, C. A. Arguello, and S. P. S. Porto, *Phys. Rev. B* **4**, 4542 (1971).
¹⁵W. Hayes and R. Loudon, *Scattering of Light by Crystals* (Wiley, New York, 1978).